LAWRENCE
LIVERMORE
NATIONAL
LABORATORY

LLNL-JRNL-648696

Disproportionation of Ag+ by pressure-and heat-induced Xe insertion into Ag-natrolite

D. Seoung, H. Cynn, C. Park, K. Y. Choi, D. A. Blom, W. J. Evans, C. C. Kao, T. Vogt, Y. Lee

January 23, 2014

Nature Chemistry

Disclaimer

27 December 2011

Title: Disproportionation of Ag^{+} by Pressure-and Heat-Induced Xe Insertion into Ag-Natrolite

Authors: Donghoon Seoung,[1] Hyunchae Cynn,[2] Changyong Park,[3] Kwang-Yong Choi,[4] Douglas A. Blom,[5] William J. Evans,[2] Chi-Chang Kao,[6] Thomas Vogt,[5] Yongjae Lee,[1]*

Affiliations:

[1]Department of Earth System Sciences, Yonsei University, Seoul 120749, Korea.

[2]High-Pressure Physics Group, Physiccal and Life Sciences, Lawrence Livermore National Laboratory, Livermore, CA 94550, USA.

[3]HPCAT, Geophysical Laboratory, Carnegie Institution of Washington, Argonne, IL 60439-4803, USA.

[4]Department of Physics, Chung-Ang University, Seoul 156-756, Korea.

[5]NanoCenter & Department of Chemistry and Biochemistry, University of South Carolina, Columbia, SC 29208, USA.

[6]Stanford Synchrotron Radiation Lightsource, SLAC National Accelerator Laboratory, Menlo Park, CA 94025, USA.

*Corresponding author. E-mail: YongjaeLee@yonsei.ac.kr

Abstract: Pressure can drastically alter chemical and physical properties of materials and allow structural phase transitions and chemical reactions to occur that defy much of our understanding gained at ambient conditions. The observation and prediction of new exotic binary phases of sodium chlorides (*1*) and the auto-dissociations of XeF_2 and NO_2 at high pressures suggests new chemistry is within reach (*2*). Particularly exciting is the high-pressure chemistry of Xenon, which has been found to react with ice (*3*) and hydrogen (*4*) and predicted to form stable Mg-Xe compounds (*5*) under pressure. We show that $Ag_{16}Al_{16}Si_{24}O_{80} \cdot 16H_2O$ inserts Xe at 1.7 GPa and 250 °C and Ag^{+} disproportionates to metallic Ag and Ag^{2+} which is retained together with Xe within the pores after pressure release. This represents the first case of Xe acting as a chemical mediator based on its adduct forming capabilities within small pores.

One Sentence Summary: Silver(I)-natrolite, $Ag_{16}Al_{16}Si_{24}O_{80} \cdot 16H_2O$, absorbs and retains ca. 28 wt.% of Xe (or 9 Xe atoms per 80 framework oxygen atoms) at 1.7 GPa and 250 °C while undergoing a charge disproportionation into divalent Ag(II) which remains in the zeolite pores and metallic silver which diffuses out of the zeolite and forms nanoparticles on the surfaces.

Main Text:

Since Bartlett's seminal discovery of $[XeF][Pt_2F_{11}]$ (*6*), Xenon's distinct chemical reactivity has led to the synthesis of hundreds of compounds (*7*) and been conjectured to be the cause of its depletion relative to other noble gases in the atmosphere of the Earth, Mars, Uranus and Neptune ("missing Xe problem"). This has led to suggestions that under certain conditions Xe becomes soluble and trapped in minerals (*8*). It is well-established that Xe forms water clathrates at ambient (*9*) and high-pressure conditions (*10*) and can be sequestered within nanometer size pores of certain zeolites (*11*).

Pioneering work by Barrer on the sorption of Xe in zeolites at high pressures and temperatures found Ag-exchanged large-pore zeolites such as X, Y, chabazite and ZSM-5 with high isosteric heats of adsorbtion (*12, 13*). Due to its large polarizability and sensitivity of NMR chemical shifts, the adsorption of Xe in zeolites is used to probe adsorption sites (*14*). Work by Sanloup et al. (*15*) suggests the formation of Xe silicates at high pressures and temperatures in laser-heated samples of Xe and β-cristobalite contained in diamond-anvil cells (DAC). It was proposed that Xe partially replaces silicon in the quartz structure (*16*). Recent theoretical work by Zhu et al. (*17*) suggests that Sanloup's experiments at pressures between 0.7 and 10 GPa point to an entropy driven insertion of Xe under pressure.

We report on pressure- and heat-induced insertion of Xe into a small pore zeolite, Ag-natrolite (Ag-NAT, $Ag_{16}Al_{16}Si_{24}O_{80} \cdot 16H_2O$) using in-situ high pressure synchrotron X-ray powder diffraction (HPXRD) in a diamond anvil cell (DAC) and ex-situ X-ray fluorescence spectroscopy (XRF) in combination with High-Angle Annular Dark Field Scanning Transmission Electron Microscopy (HAADF-STEM), energy-dispersive X-ray spectroscopy (EDS), and electron paramagnetic resonance measurements (EPR). We establish the insertion of Xe into Ag-NAT under pressure and heat and characterize the recovered phase after pressure release. Our previous work has established that pressure-induced insertion of noble gas atoms such as Ar in natrolites occurs via a 'rotating squares'-mechanism allowing the pores to widen and absorb chemical entities (*18*). We establish that the behavior of Ag-NAT at high pressures and temperatures *in the presence of Xe* is different to that when Kr is present. Both Xe- and Kr-insertion into Ag-NAT differ from Ar-insertion into Na-natrolite, where a so-called para-natrolite type phase ($Na\text{-}NAT \cdot 16H_2O \cdot 6Ar$) was found (*19*).

The HPXRD experiments were done during repeated pressurizing and heating cycles, in which the DAC was heated ex-situ in an oven and then cooled down to room temperature again. The error of the pressure measurement is estimated to be about 0.1 GPa. At the initial pressure of 1.1(1) GPa, one can clearly discern diffraction rings of Ag-NAT and solid Xe ($\mathbf{F}m\bar{3}m$, a = 5.91(1) Å) (Fig. 1A). At 1.7(1) GPa after annealing at 250 °C one observes significant changes: (i) a symmetry lowering of Ag-NAT to a monoclinic phase, (ii) formation of single crystals of solid Xe as evidenced by diffraction spots, (iii) appearance of additional diffraction lines of metallic Ag ($\mathbf{F}m\bar{3}m$, a = 4.02(1) Å) (Fig. 1A), and (iv) an expansion of the unit cell volume of monoclinic Ag-NAT by 3.2% compared to before annealing (Fig. 1B).

After pressure release and exposing the sample to ambient conditions, solid Xe reverts back to the gas phase and a monoclinic Ag-NAT phase is recovered which has a ca. 3.5% larger unit cell volume than that of the starting phase along with metallic Ag (Fig. 1A). In the recovered Ag-NAT·Xe we clearly detect the presence of Xe atoms using XRF (Fig. 2). Fig. 2A shows that the Ag-NAT·Xe phase after pressure release is still monoclinic, and when heated in air,

transforms back to the original orthorhombic one. After heating above 95°C, no further Xe is detected in the XRF spectra (Fig 2B).

We observe several chemical changes of our sample due to pressure and heating cycles *in the presence of Xe* which is inserted under pressure into the Ag-NAT pores. As evidenced by the pressure-induced expansion of the unit cell, the $Ag_{16}Al_{16}Si_{24}O_{80} \cdot 16H_2O$ orthorhombic (**F***dd2*) phase transforms into a monoclinic phase (**C***c*) with stoichiometry $Ag_{7.4}Al_{16}Si_{24}O_{80} \cdot 9.3Xe$ (Ag-NAT·Xe) above 1.7(1) GPa after annealing at 250°C. At the same conditions metallic Ag is detected. It is well-established that Ag nanoparticles form on the surfaces of Ag-exchanged chabazite under reducing conditions at temperatures as low as 150 °C (*20*) and can also be synthesized using electron beams (*21*) and ultrasound (*22*). It is noteworthy that Ag-NAT has been investigated numerous times by us using synchrotron X-rays in the presence of Ar, CO_2, various alcohol mixtures, and water at even higher pressures and temperatures, and no Ag nanoparticles have ever been found in the diffraction patterns or seen in HAADF-STEM images (*23*). We therefore exclude the role of electron- and/or X-ray beam irradiation in the Ag^+ to Ag reduction. Our HAADF-STEM images, EDS spectra and broad X-ray powder diffraction peaks from the recovered Ag-NAT·Xe sample clearly show the presence of metallic Ag nanoparticles with sizes between 5 and 25 nm with $\mathbf{F}m\bar{3}m$ symmetry and a=4.08(1) Å (Fig. 1A) formed on the outside of Ag-NAT particles as well as traces of pressure-inserted Xe (Fig. 4A).

It is intriguing that Xe is retained within Ag-NAT·Xe after pressure release and can be desorbed by heating the sample in air as shown by XRF measurements (Fig. 2B). Subsequent rehydration takes place at ambient laboratory and humidity conditions and results in a material with the composition $Ag_{7.4}Al_{16}Si_{24}O_{80} \cdot 8.6H_2O$. The detailed structural refinement results are summarized separately (Tables S1 and S2). Interestingly, the Xe-desorbed and rehydrated phase shows a very similar unit-cell volume (i.e. 0.1 % smaller) as the original phase $Ag_{16}Al_{16}Si_{24}O_{80} \cdot 16\ H_2O$ (Table S1) although both cation and water contents have been nominally halved.

In order to establish the uniqueness of Xe insertion, additional experiments have been performed using Kr as a pressure transmitting medium. In this case, similar changes were observed: at 2.1(1) GPa after annealing at 250 °C, an expanded Ag-NAT phase formed and the concomitant crystallization of metallic Ag was observed. This suggests Kr insertion into the natrolite framework and partial reduction of Ag(I) to metallic Ag (Figs. S2 and S3). However, the unit cell volume increase when inserting Kr is only about 1.2%. This expanded phase shows a marginal volume increase with further pressure increase (Fig. 1B). After pressure release and exposure to atmospheric conditions, the expanded Ag-NAT phase transforms to a phase with a unit cell volume 0.7 % smaller than the starting material coexisting with metallic Ag nanoparticles. This suggests that, unlike in the case of Xe insertion, pressure-inserted Kr atoms are readily desorbed from the natrolite pores at ambient conditions without the need for additional heating. The different chemical reactivity of Xe and Kr, also predicted in the Mg-Xe and Mg-Kr system by Miao (*5*), points to a more complex explanation of the "missing Xe problem", as it suggests distinct chemical interactions of noble gases with a plethora of phases.

Charge neutrality would require that the silver ions in the recovered Ag-NAT·Xe pores are divalent and the result of a charge-disproportionation of the original monovalent silver to metallic silver and Ag^{2+} during pressure- and heat-induced Xe insertion. This is highly unusual since this charge disproportionation has an equilibrium constant near 10^{-20} in water and at 25 °C (*24*). As Ag^{2+} is known to be one of the most powerful one-electron oxidizers and not stable in oxo environments it needs to be protected against reduction to Ag^+ by suitable ligands (*25*).

While ligand-induced disproportionation and stabilization of Ag^{2+} in aqueous solution has been reported (*24*), as have Ag(II)-C and Ag(II)-N bonds in porphyrine derivatives (*26, 27*) and mixed-valent Ag^{+}/Ag^{2+} pyrazine-based coordination polymers (*28*), Ag^{2+} has only been detected after γ-radiation in a Ag-X zeolite. Exposure to water vapor led to a subsequent disappearance of the Ag^{2+} EPR spectrum (*29*).

We therefore undertook EPR measurements in order to probe the charge state of Ag by determining the g-factors. We found no EPR signal for Ag-NAT within the resolution of our spectrometer indicating that only monovalent $4d^{10}$ Ag(I) ions are present (Figure 4B). In contrast, Ag-NAT·Xe shows a broad signal, which can be fitted by the sum of two Lorentzian profiles. Our peak fit to the EPR data resulted in two different, average g-factors; g_1=1.99(9) and g_2=2.11(5). The former g-factor, close to the free spin value, is typical for Ag^0 ($4d^{10}5s^1$) while the latter value matches the value for Ag^{2+} ($4d^9$) ions, having a more than half-filled ion with a quenched orbital moment (*30*). The respective peak-to-peak line width is given by ΔH_{pp}=74 mT and 53 mT. Their intensities are comparable indicating that the Ag-NAT·Xe sample contains nearly equal amounts of Ag^{2+} and Ag^0.

Xe is well known to have strong interactions with Ag(I) in Ag-exchanged zeolites. Munakata et al. demonstrated significant Ag(I)-Xe interactions in mordenite (*31*) and Kuznicki et al. (*32*) in Ag-ETS-10. Recent work by Daniel et al. (*33*) also revealed very strong adsorption sites in a variety of other Ag-exchanged large pore zeolites. Using density functional theory, Nguyen et al. (*34*) showed that Xe adsorption on small non-metallic silver cluster adsorbed *on* the chabazite surface can be described by a σ-donation from the 5p orbital of Xe to the 5s orbital of Ag^+ ($4d^{10}$ $5s^0$). When reduced to metallic Ag, this affinity for Xe no longer exists.

The expanded monoclinic phase at high pressure has an approximate stoichiomtery $Ag_{7.4}Al_{16}Si_{24}O_{80}$ · 9.3Xe. Kim & Seff (*35*) and Sun & Seff (*36*) report on various clusters including zero-valent Ag_6^0 in large pore Ag^+-exchanged zeolites. However, the smaller pore size in natrolites does not allow the formation of large clusters. The Ag-Xe distances of 3.2(1) and 3.1(2) Å are in the range of weak interactions commensurate with dative bonds in Xe adducts. Kurzydlowski and Grochala (*7, 37*) have proposed that Xenon's ability to form adducts under pressure might result in the stabilization of novel chemical compounds and potentially unusual oxidation states. At ambient conditions Ag^{2+} oxidizes most anions such as O^{2-} due to the large second ionization potential of Ag, which with 21.48 eV is almost identical to that of Xe with 20.98 eV (*38*). The very high polarizability of Xe can further stabilize Ag^{2+} as gas phase experiments have shown (*39*).

We show that Ag-NAT at moderate pressures and temperatures in the presence of Xe and Kr form small nanoparticles of Ag which are deposited on the outside of Ag-NAT particles and that Xe in contrast to Kr is retained within the pores after pressure release and requires heat to be desorbed. We provide EPR evidence that in Ag-NAT·Xe Ag^{2+} is present and stabilized within the pores of the small pore natrolite by Xe. This pressure and heat induced Xe insertion in Ag-NAT represents the first case of Xe acting as a chemical mediator based on its adduct forming capabilities within small pores.

References and Notes:

1. W. Zhang et al., *Science* **342**, 1502-1505 (2013).
2. W. Grochala, R. Hoffmann, J. Feng, N. W. Ashcroft, *Angew. Chem. Int. Edit.* **46**, 3620-3642 (2007).
3. C. Sanloup, S. A. Bonev, M. Hochlaf, H. E. Maynard-Casely, *Phys. Rev. Lett.* **110**, (2013).
4. M. Somayazulu et al., *Nature Chemistry* **2**, 50-53 (2010).
5. M. Miao, *arXiv e-print*, 1309.0696 (2013).
6. N. Bartlett, *P. Chem. Soc.*, (1962).
7. W. Grochala, *Chem. Soc. Rev.* **36**, 1632-1655 (2007).
8. E. Anders, T. Owen, *Science* **198**, 453-465 (1977).
9. R. M. Barrer, D. J. Ruzicka, *Trans. Faraday Soc.* **58**, 2239-2252 (1962).
10. Y. A. Dyadin et al., *J. Inclus. Phenom. Mol.* **28**, 271-285 (1997).
11. N. H. Heo et al., *J. Phys. Chem. B* **103**, 1881-1889 (1999).
12. R. M. Barrer, R. Papadopoulos, *P. R. Soc. Lond. A. Mat.* **326**, 315-330 (1972).
13. R. M. Barrer, R. Papadopoulos, J. D. F. Ramsay, *P. R. Soc. Lond. A. Mat.* **326**, 331-345 (1972).
14. T. Ito, J. Fraissard, *J. Chem. Phys.* **76**, 5225-5229 (1981).
15. C. Sanloup, R. J. Hemley, H. K. Mao, *Geophys. Res. Lett.* **29**, 30-31 (2002).
16. C. Sanloup et sl., *Science* **310**, 1174-1177 (2005).
17. Q. Zhu et al., *Nature Chemistry* **5**, 61-65 (2013).
18. D. Seoung, Y. Lee, Y. Lee, C. C. Kao, T. Vogt, *Chem. -Euro. J.* **19**, 10876-10883 (2013).
19. Y. Lee, J. A. Hriljac, T. Vogt, *J. Phys. Chem. C* **114**, 6922-6927 (2010).
20. S. M. Kuznicki et al., *Micropor. Mesopor. Mat.* **103**, 309-315 (2007).
21. Y. Sasaki, T. Suzuki, *Mater. Trans.* **50**, 1050-1053 (2009).
22. J. Talebi, R. Halladj, S. Askari, *J. Mater. Sci.* **45**, 3318-3324 (2010).
23. Y. Lee, D. Seoung, Y. N. Jang, T. Vogt, Y. Lee, *Chem. -Euro. J.* **19**, 5806-5811 (2013).
24. M. O. Kestner, A. L. Allred, *J. Am. Chem. Soc.* **94**, 7189-7190 (1972).
25. W. Grochala, *Inorg. Chem. Commun.* **11**, 155-158 (2008).
26. I. Zilbermann et al., *Electrochem. Commun.* **4**, 862-865 (2002).
27. H. Kunkely, A. Vogler, *Inorg. Chem. Commun.* **10**, 1294-1296 (2007).
28. D. Sun et al., *Chem. Commun.* **46**, 8168-8170 (2010).
29. N. Kanzaki, I. Yasumori, *J. Phys. Chem.* **82**, 2351-2352 (1978).
30. A. Abragam, B. Bleaney, *Electron Paramagnetic Resonance of Transition Ions*. (Claredon Press, Oxford, 1970).
31. K. Munakata, S. Kanjo, S. Yamatsuki, A. Koga, D. Ianovski, *J. Nucl. Sci. Technol.* **40**, 695-697 (2003).
32. S. M. Kuznicki et al., *J. Phys. Chem. C* **111**, 1560-1562 (2007).
33. C. Daniel et al., *J. Phys. Chem. C* **117**, 15122-15129 (2013).
34. H. G. Nguyen, G. Konya, E. M. Eyring, D. B. Hunter, T. N. Truong, *J. Phys. Chem. C* **113**, 12818-12825 (2009).
35. Y. Kim, K. Seff, *J. Am. Chem. Soc.* **99**, 7055-7057 (1977).
36. T. Sun, K. Seff, *Chem. Rev.* **94**, X-870 (1994).
37. D. Kurzydłowski, W. Grochala, *Z. Anorg. Allg. Chem.* **634**, 1082-1086 (2008).
38. A. Kramida, Y. Ralchenko, J. Reader. (National Institute of Standard and Technology, Gaitherburg, MD, 2013).

39. N. R. Walker, R. R. Wright, A. J. Stace, *J. Am. Chem. Soc.* **121**, 4837-4844 (1999).

Acknowledgments: This work was supported by the Global Research Laboratory Program of the Korean Ministry of Science, ICT and Planning (MSIP) and was performed under the auspices of the U.S. Department of Energy by LLNLunder contract W-7405-Eng-48 and DE-AC52-07NA27344. Experiments using synchrotron were supported by MSIP's PAL-XFEL project. A portion of this work was performed at HPCAT (Sector 16), Advanced Photon Source (APS), Argonne National Laboratory. HPCAT operations are supported by DOE-NNSA under Award No. DE-NA0001974 and DOE-BES under Award No. DE-FG02-99ER45775, with partial instrumentation funding by NSF. APS is supported by DOE-BES, under Contract No. DE-AC02-06CH11357 .

Author contributions: Y.L. and T.V. designed the research, edited and wrote the paper. D.S. performed the HPXRD experiments and structure analyses. H.C. and C.P. engineered the experiments at APS. D.B. and K.C. did the HAADF-STEM and EPR measurements, respectively. W.E. and C.K discussed the results with Y.L.

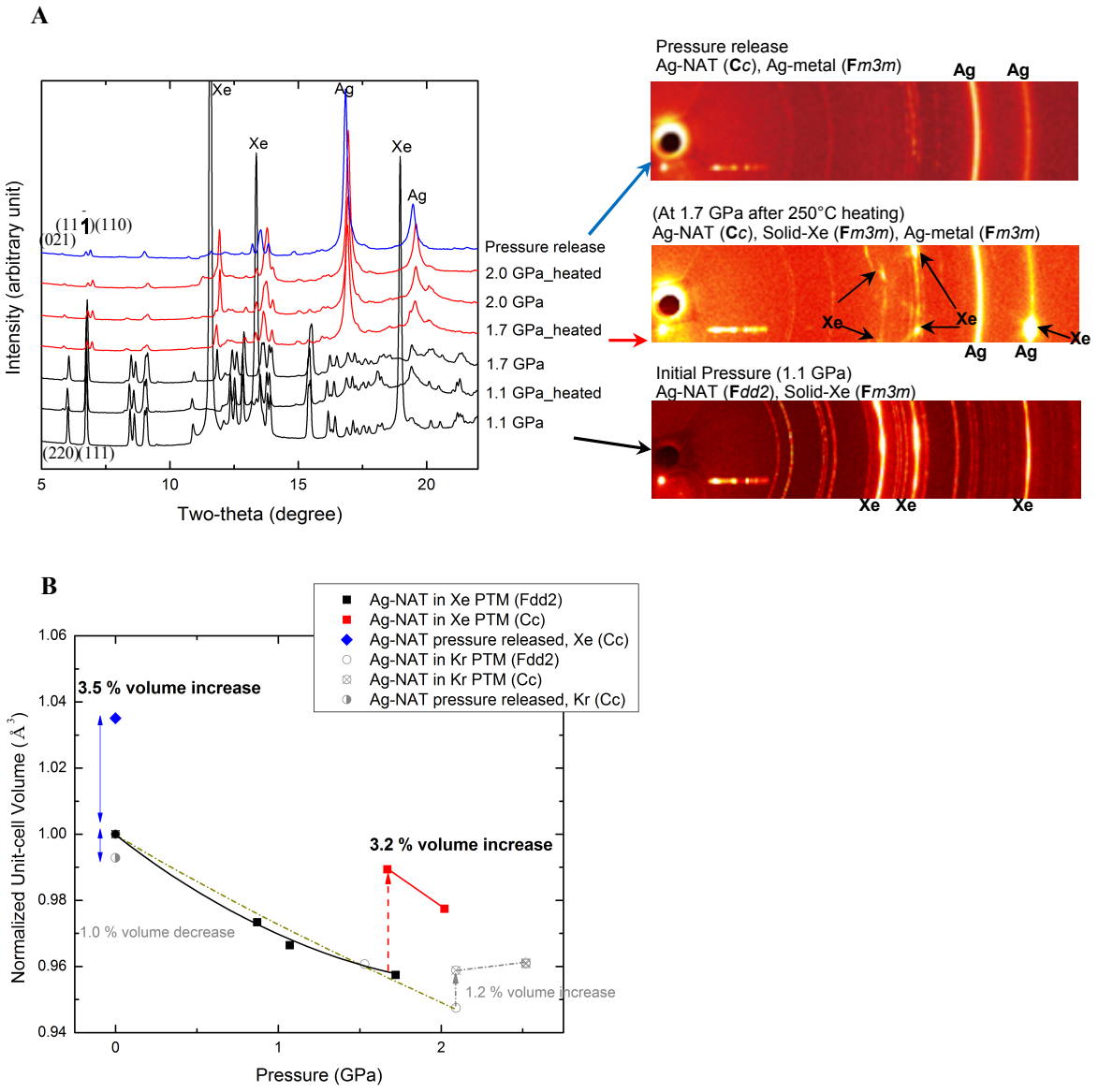

Fig. 1. (**A**) Pressure- and heat-induced changes in the synchrotron X-ray powder diffraction patterns measured for Ag-NAT using Xe as a pressure-transmitting medium. Patterns in black, red and blue colors indicate Ag-NAT in **F***dd2*, Ag-NAT in **C***c*, and Ag-NAT in **C***c* after pressure release, respectively. The heated samples were measured after quenching to ambient temperature. X-ray diffraction images at selected pressures are shown to the right to emphasize the evolution of Xe and Ag under increasing pressure. (**B**) Pressure-dependent changes of the unit-cell volume of Ag-NAT using Xe and Kr as pressure transmission media. The volumes of monoclinic phases were normalized to O_{80} (framework) to compare to those of the starting orthorhombic phase. Estimated standard deviations are smaller than the symbols.

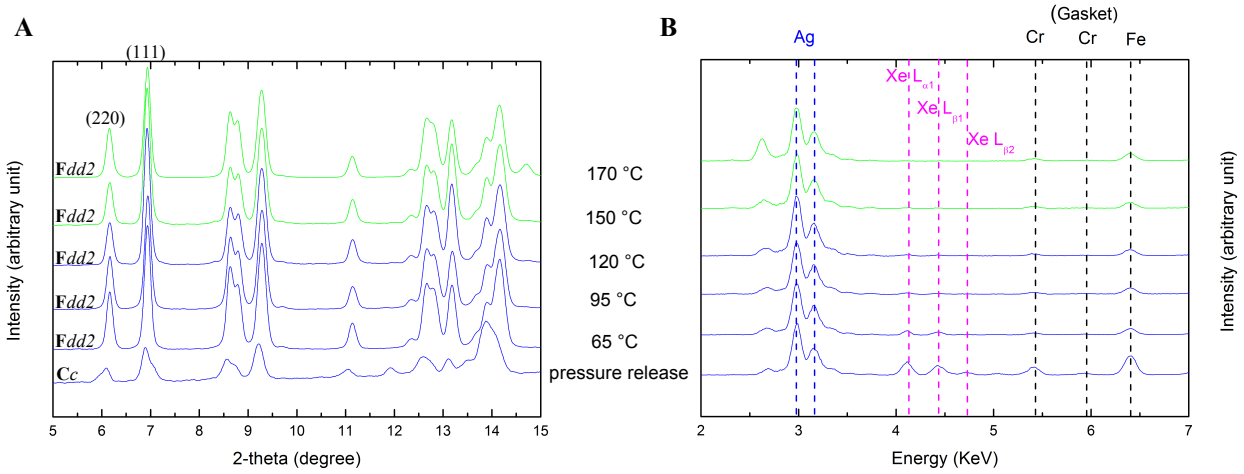

Fig. 2. Heat- induced changes in (**A**) X-ray powder diffraction patterns and (**B**) X-ray fluorescence spectra measured from the recovered Ag-NAT·Xe. The blue colored patterns represent Ag-NAT·Xe with Xe inside the pores. The vertical dashes guide the fluorescence lines from Xe (pink), Ag (blue) and the stainless steel gasket (black).

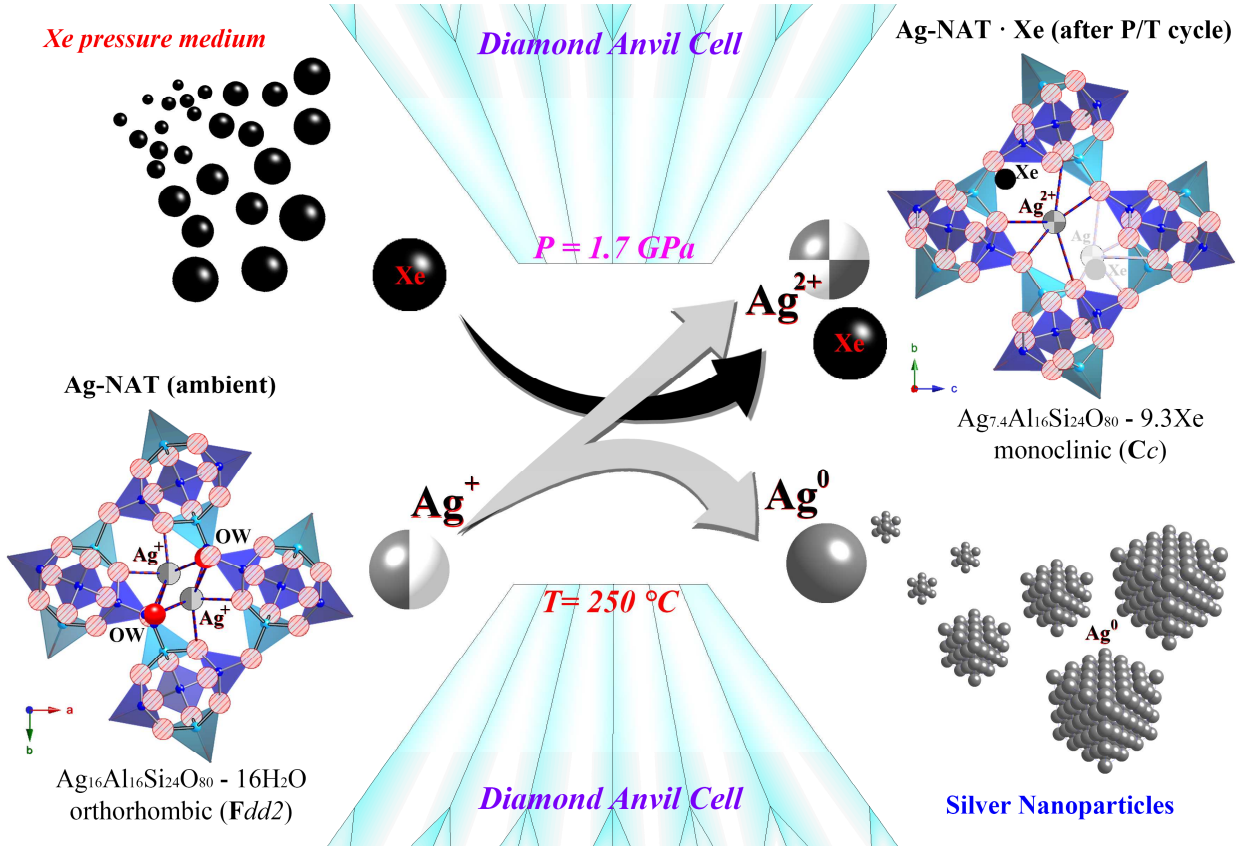

Fig. 3. Graphical representations to illustrate the conversion of Ag^{+}-containing Ag-NAT to Ag nanoparticles and Ag-NAT·Xe, after being subjected to pressure/heating cycles up to 1.7(1) GPa and 250°C. The Xe atoms are shown as rendered black balls, the monovalent silver cations as gray colored two-tone balls, the divalent silver cations as grey colored beach-balls, and the zerovalent silver metal as rendered grey balls, respectively. Water molecules are shown as rendered red balls whereas framework oxygen atoms are shown as striped red balls. Blue and azure tetrahedra represent ordered distribution of Si- and Al-tetrahedra, respectively.

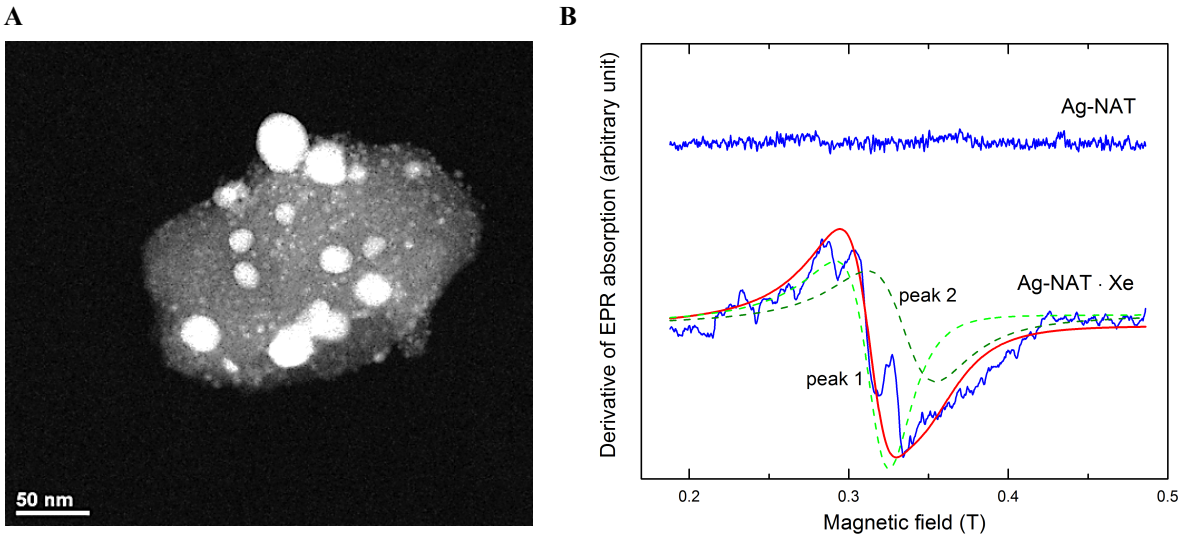

Fig. 4. (**A**) HAADF-STEM image of Ag-NAT·Xe after pressure release. Ag nanoparticles with high Z-contrast have leached out of the zeolite and are deposited on its surface. (**B**) Comparison of derivative of the EPR absorption between Ag-NAT and Ag-NAT·Xe samples measured at ν=9.44 GHz and T = 295 K. The solid red line is a fit to a sum of Lorentzian profiles (designated by peak 1 and peak 2).

Supplementary Materials:

Materials and Methods

Figures S1-S3

Tables S1-S2

References (*1-6*)

Supplementary Materials:

Materials and Methods:

The preparation of Ag-exchanged natrolite was described in detail by Lee et al (*1*). *In situ* high-pressure synchrotron X-ray powder diffraction experiment on Ag-NAT mediated by Xe was performed at the beamlines 16-BMD of HPCAT at Advanced Photon Source (APS) at Argonne National Laboratory while Kr medium experiment was performed at beamline 10C at Pohang Accelerator Laboratory (PAL). At the APS 16-BMD beamline, the primary white beam from bending magnet was monochromatized (0.6889 Å) using a Si (111) double crystal and focused by Kirkpatrick-Baez (KB) mirrors both in vertical and horizontal dimension. At the PAL 10C beamline, focussed X-ray with 0.61992 Å wavelength was used. MAR345 Image Plate was used for collecting diffraction data at both beamlines.

A modified Merrill-Bassett type diamond anvil cell (DAC) was used for the high-pressure experiments, equipped with two type-I diamond anvils with culet diameter of 800 μm and tungsten-carbide supports (*2*). A stainless-steel gasket with 250 μm thickness was pre-indented to thickness of about 100 μm, and a 500 μm diameter sample chamber was obtained by electro-spark erosion. The powdered sample was placed in the gasket hole with ruby chips for *in situ* pressure measurement. When using Xe and Kr as pressure-transmitting media (PTM), cryogenically solidified Xe and Kr were loaded on top of the packed Ag-NAT powder inside the gasket hole while DAC was partially immersed in a liquid nitrogen bath. Subsequently, the DAC was sealed and tightened at low temperatures, and the first pressure point at ambient temperature was observed to be near 1.1 GPa and 0.7 GPa for Xe and Kr, respectively. In order to ensure hydrostatic conditions at higher pressures and facilitate pressure-induced insertion, the DAC was occasionally heated at temperatures between 200 and 250 °C in an oven for 1 hour. The pressure of the sample inside the DAC was measured by detecting the shift in the R1 emission line of the included ruby balls (precision: ± 0.05 GPa) (*3*). The sample was equilibrated typically for about 10 minutes in the DAC at each measured pressure. After each powder diffraction pattern was collected, the pressure was increased with ca. 0.5(1) GPa increment up to 2.0(1) GPa in the case of Xe PTM (up to 2.5GPa for Kr). After each set of experiments with different PTM, a final data set was measured after releasing the pressure and exposing the sample to ambient condition for an hour.

Pressure-dependent changes of the unit-cell lengths and volumes were derived from a series of full profile fitting procedures using the GSAS program suite (*4*). The background was fitted using a Chebyshev polynomial with ≤ 20 coefficients, and the pseudo-Voigt profile function proposed by Thompson et al. was used to model the observed Bragg peaks (*5*). The structural models at selected pressures were then established by Rietveld methods (*6*). In order to

reduce the number of variables, isotropic displacement factors for the ambient pressure models were refined by grouping the framework tetrahedral atoms, framework oxygen atoms, and non-framework cations and water oxygen atoms, respectively. For the high-pressure models, all the isotropic displacement factors were grouped to be same. Geometrical soft-restraints on the T-O (T = Si, Al) and O-O bond distances of the tetrahedra were applied: the distances between Si-O and Al-O were restrained to target values of 1.620 ± 0.001Å and 1.750 ± 0.001Å, respectively, and the O-O distances to 2.646 ± 0.005Å for the Si-tetrahedra and 2.858 ± 0.005Å for the Al-tetrahedra. The distribution of the non-framework species in the pores was established using successive difference Fourier syntheses. In the final stages of the refinements, the weights of the soft-restraints were gradually reduced, which did not lead to any significant changes of the inter-atomic distances. The final convergence of the refinement was achieved by varying simultaneously all background and profile parameters, scale factor, lattice constants, 2θ zero, and the atomic positional, fractional, and displacement parameters (Table S1).

Micro X-ray fluorescence spectrometer (XRF, M4 Tornado, Bruker) at Department of Earth System Sciences at Yonsei University was used to detect the confined Xe atoms from the recovered Ag-NAT phase and their desorption after successive heating. The system was operated using a micro focused X-ray with 25 μm beamsize by polycapillary optics. Rhodium target was used to generate the X-ray at an accelerating voltage of 50 KV and a current of 200 μA.

Scanning transmission electron microscopy (STEM) was used to image the recovered Ag-NAT phase with a JEOL 2100F 200kV FEG-STEM/TEM equipped with a CEOS C_s corrector on the illumination system. The geometrical aberrations were measured and controlled to provide less than a π/4 phase shift of the incoming electron wave over the probe-defining aperture of 17.5 mrad. High angle annular dark-field (HAADF) STEM images were acquired on a Fischione Model 3000 HAADF detector with a camera length such that the inner cut-off angle of the detector was 75 mrad. The scanning acquisition was synchronized to the 60 Hz AC electrical power to minimize 60Hz noise in the images and a pixel dwell time of 24μs was used.

Room temperature Electron Paramagnetic Resonance experiments were performed at an X-band (ν=9.44 GHz) using a JEOL JESFA200 spectrometer. In the Ag-NAT·Xe sample, the observed Lorentzian line-shape means that the EPR signal is exchange-narrowed due to fast electronic fluctuations of Ag ions. The lack of sharp satellite peaks arising from hyperfine interactions with the surrounding nuclei rules out the presence of isolated, paramagnetic Ag ions

1. Y. Lee, D. Seoung, Y. Lee, *Am. Mineral.* **96**, 1718-1724 (2011)
2. H. O. K. Mao, R. J. Hemley, *Philos. T. R. Soc. A* **354**, 1315-1332 (1996)
3. P. M. Bell, H. K. Mao, *Carnegie Institution of Washington Yearbook*. (Carnegie Institute, Washington, DC, 1979), **78**, pp. 665-669.
4. B. H. Toby, *J. Appl. Crystallogr.* **34**, 210-213 (2001)
5. P. Thompson, D. E. Cox, J. B. Hastings, *J. Appl. Crystallogr.* **20**, 79-83 (1987)
6. H. M. Rietveld, *J. Appl. Crystallogr.* **2**, 65-71 (1969)

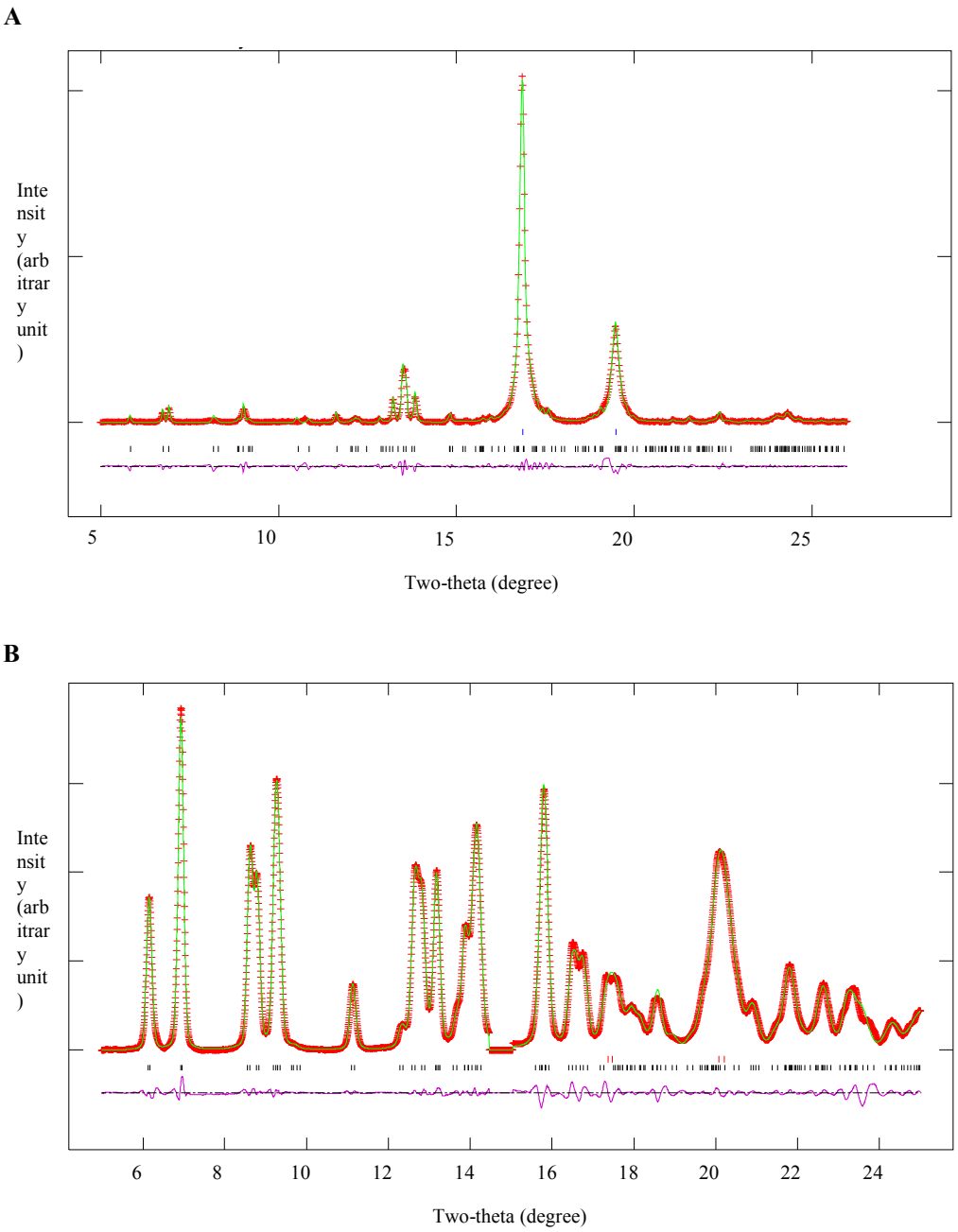

Fig. S1. Final Rietveld refinement fits between the observed (cross) and calculated (line) profiles for Ag-NAT (a) after P/T cycle of Xe PTM run measured at 16-BM-D beamline at APS (λ=0.6889Å) and (b) after *ex situ* heating to induce Xe-desorption measured using in-house XRD at Yonsei University (Mo Kα1 : Kα2 = 2:1). The difference curve is shown below in the same scale, and the positions of the Bragg reflections from Ag-NAT (**C***c*) and metallic silver (**F**$m\bar{3}m$) are marked as vertical bars.

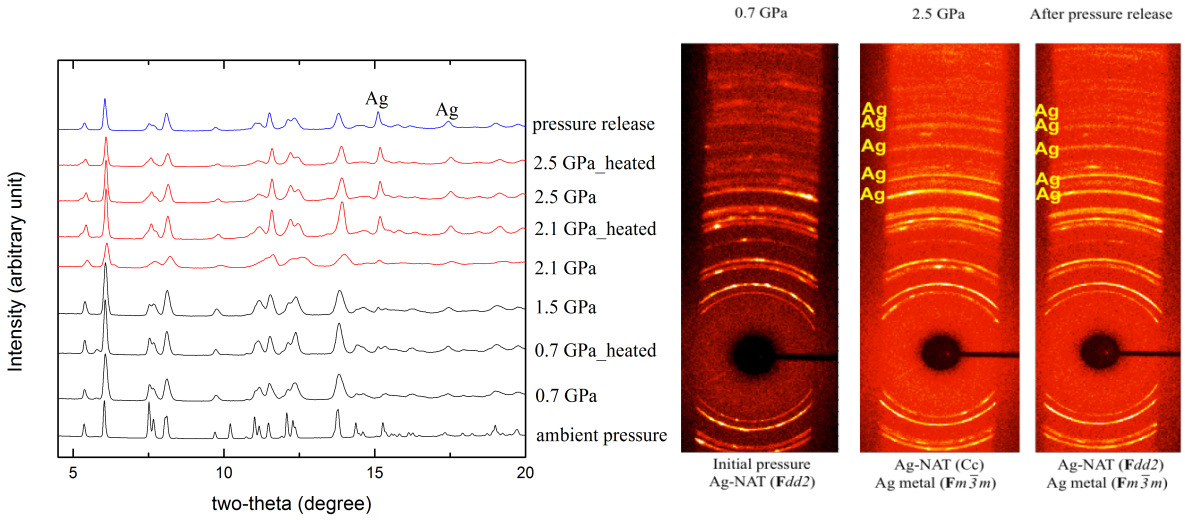

Fig. S2. Pressure- and heat-induced changes in the X-ray powder diffraction patterns of Ag-NAT using Kr as PTM at PAL.

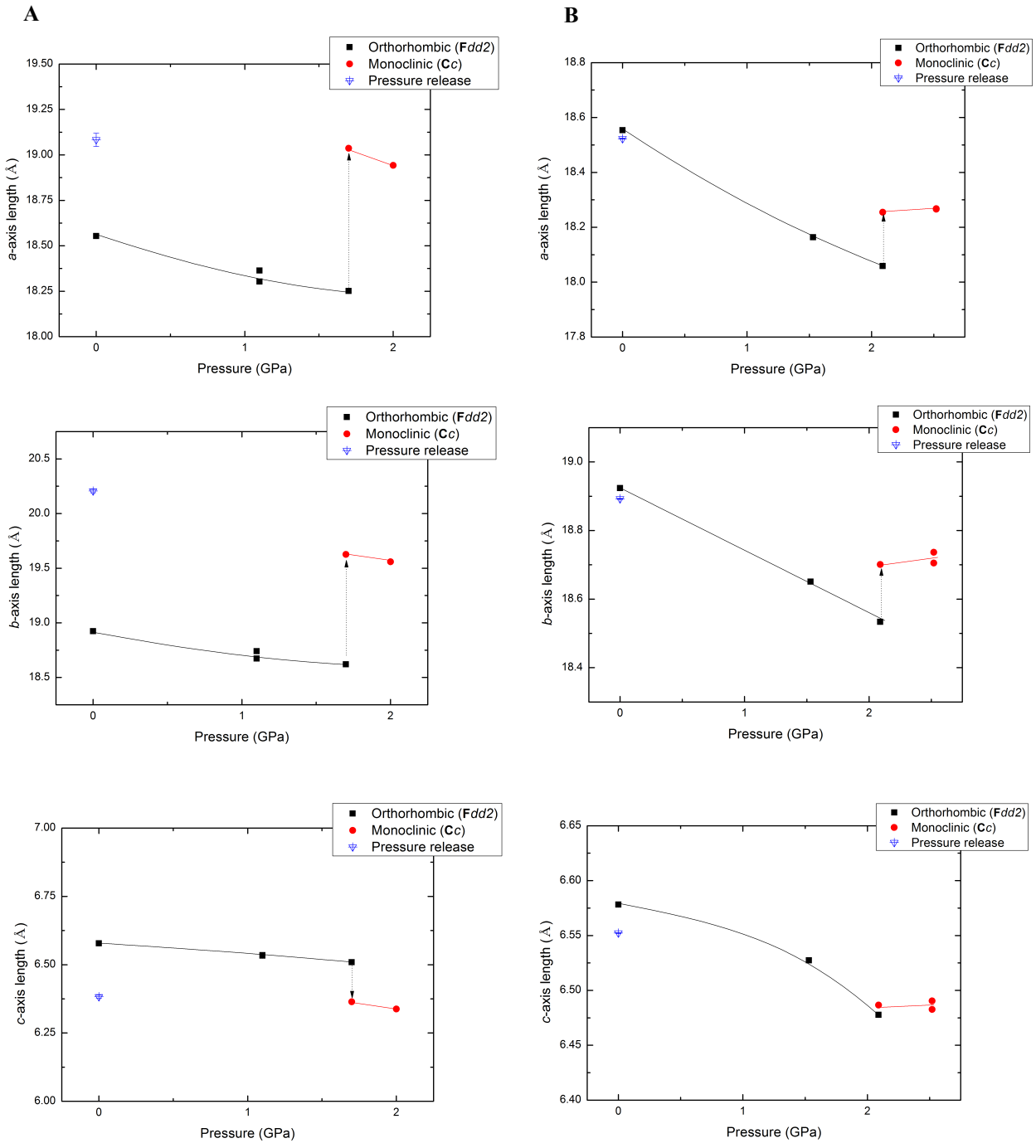

Fig. S3. Changes in the unit-cell lengths (Å) of Ag-NAT as a function of pressure mediated by (**A**) Xe and (**B**) Kr . Lines are guides to eyes. The unit-cell lengths of the monoclinic (**C***c*) phase are converted to orthorhombic (**F***dd2*) scale for easy comparison.

Table S1. Final refined atomic coordinates of Ag-NAT at ambient condition, after P/T cycle in Xe PTM run, and after 170 °C heating, respectively.[a]

		Starting phase[b,d]	After P,T cycle[c]	After heating at 170 °C [b]
Space group		**F***dd2*	**C***c*	**F***dd2*
$_wR_p$(%), χ^2		4.33, 4.52	2.22, 0.743	12.1, 4.59
Cell parameter (Å)	*a*	18.5538(1)	6.382(6)	18.559(2)
	b	18.9238(1)	19.08(4)	18.912(2)
	c	6.5782(1)	10.10(2)	6.572(1)
	beta		105.94(5)	
Cell volume (Å^3)	*V*	2309.64(3)	1183.0(4)	2306.9(7)
Si(1)	*x*	0	0.483(4)	0
8a (**F***dd2*)	*y*	0	0.3746(3)	0
4a (**C***c*)	*z*	0.0288(5)	-0.018(5)	0.0107(4)
Si(2)	*x*	0.1550(1)	0.198(4)	0.1547(2)
16b (**F***dd2*)	*y*	0.2092(1)	0.3293(2)	0.2135(1)
4a(**C***c*)	*z*	0.6468(3)	0.179(5)	0.6276(4)
Si(3)	*x*		0.559(4)	
	y		0.0798(3)	
4a (**C***c*)	*z*		0.332(5)	
Al(1)	*x*	0.0390(1)	0.929(4)	0.0383(1)
16b (**F***dd2*)	*y*	0.0917(1)	0.4583(3)	0.0918(2)
4a (**C***c*)	*z*	0.6431(3)	0.096(5)	0.6229(4)
Al(2)	*x*		0.347(4)	
	y		0.2181(2)	
4a (**C***c*)	*z*		0.425(5)	
O(1)	*x*	0.0285(3)	0.563(4)	0.0146(3)
16b (**F***dd2*)	*y*	0.0666(1)	0.0336(4)	0.06890(8)
4a(**C***c*)	*z*	0.8962(4)	0.467(5)	0.8703(5)
O(2)	*x*	0.0749(2)	0.457(4)	0.0762(2)
16b (**F***dd2*)	*y*	0.1767(2)	0.0357(4)	0.1760(2)
4a(**C***c*)	*z*	0.6298(8)	0.192(5)	0.6187(6)
O(3)	*x*	0.0976(2)	0.408(4)	0.1004(2)
16b (**F***dd2*)	*y*	0.0340(2)	0.1485(4)	0.0320(2)
4a(**C***c*)	*z*	0.5174(6)	0.329(5)	0.5249(7)
O(4)	*x*	0.2080(2)	0.103(4)	0.2119(2)
16b (**F***dd2*)	*y*	0.1539(2)	0.1981(4)	0.1575(2)
4a(**C***c*)	*z*	0.7587(6)	0.464(5)	0.7194(8)
O(5)	*x*	0.1826(2)	0.323(4)	0.17963(8)
16b (**F***dd2*)	*y*	0.2231(2)	0.2942(3)	0.2372(3)
4a(**C***c*)	*z*	0.4163(4)	0.325(5)	0.4016(4)
O(6)	*x*		0.055(4)	
	y		0.2707(3)	
4a(**C***c*)	*z*		0.077(5)	
O(7)	*x*		0.369(4)	

)	*y*		0.3645(6)	
4a(**C***c*)	*z*		0.106(5)	
O(8)	*x*		0.039(4)	
	y		0.3898(4)	
4a(**C***c*)	*z*		0.208(5)	
O(9)	*x*		0.803(4)	
	y		0.1062(6)	
4a(**C***c*)	*z*		0.339(5)	
O(10)	*x*		0.654(4)	
	y		0.4392(6)	
4a(**C***c*)	*z*		0.020(5)	
Ag(1)	*x*	0.2216(4)	0.23(4)	0.2190(2)
16b (**F***dd2*)	*y*	0.0304(4)	0.19(1)	0.0334(2)
4a(**C***c*)	*z*	0.6483(3)	0.16(4)	0.637(1)
	Occu.	0.974(2)	0.42(5)	0.46
Ag(2)	*x*		0.51(2)	
16b (**F***dd2*)	*y*		0.389(9)	
4a(**C***c*)	*z*		0.48(3)	
	Occu.		0.50(9)	
OW(1)	*x*	0.0623(3)		0.135(1)
16b (**F***dd2*)	*y*	0.1810(3)		0.1718(8)
4a(**C***c*)	*z*	0.135(1)		0.199(3)
	Occu.	1		0.67(1)
Xe(1)	*x*		0.56(2)	
16b (**F***dd2*)	*y*		0.49(1)	
4a(**C***c*)	*z*		0.25(2)	
	Occu.		0.52(7)	
Xe(2)	*x*		0.75(2)	
16b (**F***dd2*)	*y*		0.224(5)	
4a(**C***c*)	*z*		0.17(2)	
	Occu.		0.64(7)	

[a]ESD's are in parentheses.

[b]Isotropic displacement factors (U_{iso}) were refined by grouping.

[c]U_{iso}'s fixed to the values of the previous model.

[d]The atomic coordinates of the ambient model are from the previous work by Y. Lee et. al. (2011).

Table S2. Selected interatomic distances and angles of Ag-NAT at ambient condition, after P/T cycle in Xe PTM run, and after 170 °C heating, respectively.[a]

	Starting phase[c]		After P,T cycle		After heating at 170 °C
Space group	**F***dd2*		**C***c*		**F***dd2*
Si(1) - O(1)	1.622(1) x 2	Si(1) - O(4)	1.620(3)	Si(1) - O(1)	1.6194(5) x 2
Si(1) - O(5)	1.625(1) x 2	Si(1) - O(7)	1.620(2)	Si(1) - O(5)	1.6193(5) x 2
mean[b]	1.624(1)	Si(1) - O(9)	1.620(2)	mean[b]	
		Si(1) - O(10)	1.620(2)		
		mean[b]			
Si(2) - O(2)	1.612(2)	Si(2) - O(5)	1.620(2)	Si(2) - O(2)	1.6200(7)
Si(2) - O(3)	1.624(2)	Si(2) - O(6)	1.620(2)	Si(2) - O(3)	1.6188(7)
Si(2) - O(4)	1.613(2)	Si(2) - O(7)	1.620(2)	Si(2) - O(4)	1.6184(7)
Si(2) - O(5)	1.622(2)	Si(2) - O(8)	1.620(2)	Si(2) - O(5)	1.6183(7)
mean[b]	1.618(1)	mean[b]		mean[b]	
		Si(3) - O(1)	1.620(2)		
		Si(3) - O(2)	1.620(2)		
		Si(3) - O(3)	1.620(2)		
		Si(3) - O(9)	1.620(2)		
		mean[b]			
Al - O(1)	1.743(2)	Al(1) - O(1)	1.750(2)	Al - O(1)	1.7396(7)
Al - O(2)	1.743(2)	Al(1) - O(2)	1.750(3)	Al - O(2)	1.7418(7)
Al - O(3)	1.748(2)	Al(1) - O(8)	1.750(2)	Al - O(3)	1.7396(7)
Al - O(4)	1.746(2)	Al(1) - O(10)	1.750(2)	Al - O(4)	1.7399(7)
mean[b]	1.745(1)	mean[b]		mean[b]	
		Al(2) - O(3)	1.750(2)		
		Al(2) - O(4)	1.750(2)		
		Al(2) - O(5)	1.750(3)		
		Al(2) - O(6)	1.750(2)		
		mean[b]			
Si(1) - O(1) - Al	139.7(3)	Si(3) - O(1) - Al(1)	132.8(4)	Si(1) - O(1) - Al	140.1(2)
Si(2) - O(2) - Al	134.5(2)	Si(3) - O(2) - Al(1)	151.6(6)	Si(2) - O(2) - Al	140.3(2)
Si(2) - O(3) - Al	139.2(3)	Si(3) - O(3) - Al(2)	145.7(6)	Si(2) - O(3) - Al	135.7(3)
Si(2) - O(4) - Al	136.5(3)	Si(1) - O(4) - Al(2)	133.8(5)	Si(2) - O(4) - Al	136.6(3)
Si(1) - O(5) - Si(2)	144.4(3)	Si(2) - O(5) - Al(2)	144.3(5)	Si(1) - O(5) - Si(2)	142.3(2)
		Si(2) - O(6) - Al(2)	129.3(4)		
		Si(1) - O(7) - Si(2)	154.3(8)		
		Si(2) - O(8) - Al(1)	125.0(4)		
		Si(1) - O(9) - Si(3)	123.3(4)		
		Si(1) - O(10) - Al(1)	142.3(8)		
Ag(1) - O(2)	2.579(5)	Ag(1) - O(3)	2.4(3)	Ag(1) - O(2)	2.632(7)
	2.778(5)	Ag(1) - O(5)	2.5(3)		2.835(8)
Ag(1) - O(3)	2.458(4)			Ag(1) - O(3)	2.329(6)

Ag(1) - O(4)	2.460(4)	Ag(2) - O(5)	2.5(2)	Ag(1) - O(4)	2.381(6)
		Ag(2) - O(6)	3.2(2)		
OW(1) - O(1)	2.746(7)	Xe(1) - O(2)	2.9(2)	OW(1) - O(1)	3.02(2)
OW(1) - O(5)	3.006(7)	Xe(1) – O(7)	2.9(2)		2.71(2)
		Xe(1) – O(10)	2.7(2)	OW(1) - O(5)	2.69(2)
			3.0(2)		
OW(1) - Ag(1)	2.523(6)	Xe(2) – O(4)	2.5(2)	OW(1) - Ag(1)	3.18(2)
	2.523(6)	Xe(2) – O(6)	2.5(2)		3.55(2)
		Xe(2) – O(9)	2.8(2)		
		Ag(1) – Xe(2)	3.2(2)		
			3.3(3)		
		Ag(2) – Xe(1)	3.1(2)		
			3.5(2)		

[a]ESD's are in parentheses.

[b]Standard deviations computed using $\sigma = 1/n[\sum_{i=1}^{n}\sigma_i{}^2]^{1/2}$

[c]The interatomic distances of the ambient model are from the previous work by Y. Lee et. al. (2011).